GEOPHYSICS. VOL. 76, NO. 6 (NOVEMBER-DECEMBER 2011); P. D11–D19, 11 FIGS., 2 TABLES.
10.1190/GEO2010-0415.1

Estimation of shear-wave interval attenuation from mode-converted data

Bharath Shekar[1] and Ilya Tsvankin[1]

ABSTRACT

Interval attenuation measurements provide valuable information for reservoir characterization and lithology discrimination. We extend the attenuation layer-stripping method of Behura and Tsvankin to mode-converted (PS) waves with the goal of estimating the S-wave interval attenuation coefficient. By identifying PP and PS events with shared ray segments and applying the PP + PS = SS method, we first perform kinematic construction of pure shear (SS) events in the target layer and overburden. Then, the modified spectral-ratio method is used to compute the effective shear-wave attenuation coefficient for the target reflection. Finally, application of the dynamic version of velocity-independent layer stripping to the constructed SS reflections yields the interval S-wave attenuation coefficient in the target layer. The attenuation coefficient estimated for a range of source-receiver offsets can be inverted for the interval attenuation parameters. The method is tested on multicomponent synthetic data generated with the anisotropic reflectivity method for layered VTI (transversely isotropic with a vertical symmetry axis) and orthorhombic media.

INTRODUCTION

Attenuation analysis provides seismic attributes sensitive to the physical properties of the subsurface. Reliable attenuation measurements have become feasible with acquisition of high-quality reflection and borehole data. Attenuation is often found to be anisotropic (directionally dependent) due to a variety of factors, such as the intrinsic anisotropy of the material (Prasad and Nur, 2003), the presence of aligned fluid-filled fractures (Chapman, 2003; Batzle et al., 2005), or interbedding of thin layers with different properties (Carcione, 1992; Zhu et al., 2007). The magnitude of attenuation anisotropy can be much higher than that of velocity anisotropy, and the symmetry of the attenuation coefficient can be different than that of the velocity function (Liu et al., 2007; Zhu et al., 2007).

The quality factors Q_P and Q_S are widely used as measures of P- and S-wave intrinsic attenuation, respectively. Klimentos (1995) estimates compressional and shear attenuation from sonic logs in sandstone formations with variable oil, water, and gas saturation and observes that Q_P and Q_S can be used for pore-fluid discrimination. According to the results of Adam et al. (2009), the substitution of light hydrocarbons with brine in carbonate rocks leads to a large increase in P-wave attenuation. Chichinina et al. (2009) conduct ultrasonic laboratory experiments for VTI models. Their results show that the symmetry-axis attenuation of P-waves is much greater than that of S-waves in dry samples, whereas for oil-saturated samples, the two modes have comparable attenuation. Blanchard et al. (2010) correlate the time-lapse changes in P-wave attenuation measured over a carbon-sequestration site to the changes in CO_2 concentration. Shear-wave attenuation in heavy oils is closely linked to temperature and could be useful in seismic monitoring of thermal recovery processes (Behura et al., 2007). Attenuation due to the presence of gas in the near-surface layers causes distortions in the amplitudes of migrated events, which necessitates application of offset-dependent attenuation correction (Xin et al., 2008).

De et al. (1994) report measurements of the S-wave quality factor from vertical seismic profiling (VSP) surveys and sonic logs. Shear-wave attenuation is more difficult to evaluate from reflection data due to such problems as a low signal-to-noise ratio and statics errors. Behura and Tsvankin (2009a) combine the velocity-independent layer stripping (VILS) method of Dewangan and Tsvankin (2006) with the spectral-ratio method (Johnston and Toksöz, 1981) to estimate the interval attenuation of pure PP or SS reflected waves. Their method assumes the overburden layers to be laterally homogeneous with a horizontal symmetry plane, whereas the target layer can be arbitrarily anisotropic and heterogeneous. They identify the overburden and target events that share ray segments in the overburden to compute the interval traveltime and then the interval attenuation coefficient in the target. The algorithm of Behura and Tsvankin (2009a) is data-driven, and does not require information about the velocity or attenuation in the overburden. Reine

Manuscript received by the Editor 22 December 2010; revised manuscript received 26 April 2011; published online 30 December 2011.
[1]Colorado School of Mines, Department of Geophysics, Center for Wave Phenomena, Golden, Colorado, USA. E-mail: bshekar@mymail.mines.edu; ilya@dix.mines.edu.

et al. (2009a) introduce a similar algorithm for evaluating the interval P-wave attenuation. Their method operates in the τ-ρ domain and, therefore, is limited to laterally homogeneous target layers.

Shear waves, however, cannot be excited offshore, and shear-wave sources are seldom used on land. Therefore, here we extend the technique of Behura and Tsvankin (2009a) to mode-converted data by supplementing it with the PP + PS = SS method of Grechka and Tsvankin (2002). First, we discuss how the PP + PS = SS method can be combined with VILS to construct SS-wave moveout in the target layer and overburden from PP and PS data. Then the interval S-wave attenuation coefficient is obtained by extending the kinematic construction procedure to frequency-domain amplitudes processed using the spectral-ratio method. Finally, we apply the algorithm to synthetic data from layered VTI and orthorhombic media to assess the accuracy of the inversion for the SV-wave attenuation-anisotropy parameters.

METHODOLOGY

Our method operates with pure (PP) and mode-converted (PS) reflections for a medium with an arbitrarily anisotropic, heterogeneous target layer overlaid by a laterally homogeneous overburden with a horizontal symmetry plane in each layer. For simplicity, the method is described for 2D models, in which the vertical incidence plane containing sources and receivers is supposed to be a plane of mirror symmetry. Therefore, both rays and the corresponding phase-velocity vectors (PSVs) are confined to the incidence plane, and converted waves represent in-plane polarized PSV modes. The P-to-S conversion for all reflection events is assumed to occur only at the reflector. For wide-azimuth data, the split mode-converted waves have to be separated for each offset and azimuth, which, in general, requires application of Alford-type rotation (Gaiser, 1997; Dellinger et al., 2002; Simmons, 2009). We begin by introducing the kinematic algorithm designed to compute the interval shear-wave traveltimes and then describe estimation of the interval shear-wave attenuation coefficient in the target layer.

Kinematic layer stripping for interval shear-wave traveltimes

To estimate the interval shear-wave traveltimes, the PP + PS = SS method can be combined with velocity-independent layer stripping developed by Dewangan and Tsvankin (2006). Suppose P-wave sources and receivers of both P- and S-waves are continuously distributed along the acquisition line. As discussed by Grechka and Tsvankin (2002) and shown in Figure 1, matching time slopes on common-receiver gathers at the source location A allows us to identify the PP (*ARB*) and PS (*ARC*) target events that share the downgoing segment *AR* and the reflection point R at the bottom of the target layer. Likewise, for a P-wave source at B, we find PP (*BRA*) and PS (*BRD*) target events that share the downgoing segment *BR*. This procedure makes it possible to construct the SS reflection *DRC*, where C and D are the coordinates of S-wave receivers. For brevity, we denote the PP (*ARB*) and PS (*ARC* and *BRD*) events by PP_E, PS_{E1}, and PS_{E2} (respectively) and the constructed SS event *DRC* by SS_E ("E" refers to "effective" reflections from the bottom of the target layer). The exact traveltime of the reflection SS_E is (Grechka and Tsvankin, 2002)

$$t_{SS_E} = t_{PS_{E1}} + t_{PS_{E2}} - t_{PP_E}. \tag{1}$$

The constructed event SS_E can be treated (in a kinematic sense) as a pure reflection mode excited by a shear-wave source.

Next, we find the interval SS-wave traveltime in the target layer, which requires knowledge of the shear traveltimes in the overburden. Because the data are assumed to be generated with a P-wave source, it is necessary to apply the PP + PS = SS method repeatedly to construct SS reflections in the overburden (Figure 2). To layer-strip the segment *DR* of the SS-wave, we need to obtain the coordinate of point I and the traveltime along the overburden segment *ID*. Note that the horizontal slowness along any ray in the laterally homogeneous overburden is preserved.

First, we form a common-receiver gather of the PS-wave at location D (Figure 2a) and identify the point E (i.e., the location of P-wave source) where the time slope (horizontal slowness) coincides with that at D. The obtained overburden PS event *EID* shares the segment *ID* with the target SS event *CJRID*. Then we form a common-source PP gather at location E (Figure 2a) and identify the receiver location F where the time slope (horizontal slowness) coincides with that at E (and hence at D). Because the horizontal slowness does not change along each ray in the overburden, the PP reflection recorded at F shares the downgoing segment *EI* with the PS event *EID*.

Under our assumptions, the moveout function of the overburden PS event is symmetric with respect to zero offset, so the PS-wave traveltime and ray parameter remain the same when the source and receiver are interchanged. Therefore, the offset of the PS event *FIG*, which has the same reflection point and ray parameter as events *EIF* and *EID*, should coincide with that of the "reciprocal" PS reflection *EID*. The horizontal coordinate of the receiver at point G can then be found from

$$x_G = x_E + x_F - x_D. \tag{2}$$

The constructed event *DIG* (denoted by SS_{O1}, where "O" refers to the overburden and "1" to the left segment of the target SS event in Figure 2b) shares the segment *DI* with the target SS event *DRC* (Figure 2b). The PP event *EIF* will be denoted by PP_{O1} and the PS events *EID* and *FIG* by PS_{O1}. The traveltime of the event SS_{O1} is then given by

$$t_{SS_{O1}} = 2\,t_{PS_{O1}} - t_{PP_{O1}}, \tag{3}$$

and the lateral coordinate of point I is

$$x_I = \frac{x_D + x_G}{2}. \tag{4}$$

Likewise, the PP + PS = SS method can be applied to construct the overburden SS event *HJC* (SS_{O2}) that shares the segment *JC* with the target event SS_E (Figure 3). The corresponding traveltime $t_{SS_{O2}}$ and the lateral coordinate of point J are obtained using the algorithm discussed above. Hence, we can find the interval shear-wave traveltime in the target layer as

$$t_{SS_T} = t_{SS_E} - \frac{1}{2}\left(t_{SS_{O1}} + t_{SS_{O2}}\right). \tag{5}$$

The traveltime t_{SS_T} corresponds to the raypath *IRJ* of the target event SS_T. Note that the depth of the bottom of the overburden remains unknown prior to velocity analysis.

For horizontal, laterally homogeneous target layers, the ray parameter is preserved along the entire raypath of the reflection SS_E. If

the target layer also has a horizontal symmetry plane, the raypaths of the downgoing and upgoing overburden events are symmetric with respect to the vertical. Then $t_{SS_{O1}} = t_{SS_{O2}}$, and it is sufficient to apply the layer-stripping procedure just to one of the overburden segments of the target event SS_E.

Layer stripping for interval shear-wave attenuation

Behura and Tsvankin (2009a) combine VILS with the spectral-ratio method and apply their attenuation layer-stripping algorithm to frequency-domain amplitudes of pure-mode reflections. Our goal is to extend this technique to the combination of PP- and PS-waves analyzed above. The ray-theoretic frequency-domain amplitudes of the waves PP_E, PS_{E1} and PS_{E2} (Figure 1) can be written as

$$|U_{PP_E}| = S(\omega)\, \mathcal{G}_{PP_E} e^{-k^I_{P,AR} l_{AR} - k^I_{P,BR} l_{BR}}, \quad (6)$$

$$|U_{PS_{E1}}| = S(\omega)\, \mathcal{G}_{PS_{E1}} e^{-k^I_{P,AR} l_{AR}}\, e^{-k^I_{S,RC} l_{RC}}, \quad (7)$$

$$|U_{PS_{E2}}| = S(\omega)\, \mathcal{G}_{PS_{E2}} e^{-k^I_{P,BR} l_{BR}}\, e^{-k^I_{S,RD} l_{RD}}, \quad (8)$$

where $S(\omega)$ is the spectrum of the source wavelet, and $k^I_{P,XY}$ and $k^I_{S,XY}$ are the average P- and S-wave group attenuation coefficients (respectively) along the raypath XY with the length l_{XY}. The coefficients $\mathcal{G}_{PP_E}$, $\mathcal{G}_{PS_{E1}}$, and $\mathcal{G}_{PS_{E2}}$ include the source radiation pattern and receiver directivity, the reflection/transmission coefficients along the raypath, and the geometric spreading of the corresponding event. Equations 6, 7, and 8 can be combined in the following way to compute the attenuation coefficient of the reflection SS_E constructed by the PP + PS = SS method

$$|U_{SS_E}| = \frac{|U_{PS_{E1}}||U_{PS_{E2}}|}{|U_{PP_E}|} = \mathcal{G}_E\, S(\omega)\, e^{-k^I_{S,RD} l_{RD} - k^I_{S,RC} l_{RC}}, \quad (9)$$

where the ratio $\mathcal{G}_E = (\mathcal{G}_{PS1_E}\mathcal{G}_{PS2_E})/\mathcal{G}_{PP_E}$ is assumed to be independent of frequency. It should be noted that $|U_{SS_E}|$ in equation 9 does not represent the actual amplitude of the primary SS reflection. Whereas the PP + PS = SS method reproduces the kinematics of shear-wave primaries, it cannot yield the true amplitudes without knowledge of the velocity model (Grechka and Tsvankin, 2002; Grechka and Dewangan, 2003). Equation 9 can be used to evaluate effective S-wave attenuation by computing the slope of $\ln|U_{SS_E}|$ expressed as a function of ω. This operation, however, is hampered by the need to estimate the source spectrum $S(\omega)$, which is often difficult to do in practice.

However, as shown below, $S(\omega)$ is eliminated in the computation of the interval S-wave attenuation coefficient. The ray-theoretic frequency-domain amplitudes of the waves PP_{O1} and PS_{O1} (Figure 2) can be written as

$$|U_{PP_{O1}}| = S(\omega)\, \mathcal{G}_{PP_{O1}} e^{-k^I_{P,O1}(l_{EI}+l_{IF})} = S(\omega)\, \mathcal{G}_{PP_{O1}} e^{-2k^I_{P,O1} l_{EI}}, \quad (10)$$

$$|U_{PS_{O1}}| = S(\omega)\, \mathcal{G}_{PS_{O1}} e^{-k^I_{P,O1} l_{EI}}\, e^{-k^I_{S,O1} l_{ID}}, \quad (11)$$

where $k^I_{P,O1}$ and $k^I_{S,O1}$ are the average P-wave and S-wave group attenuation coefficients along the corresponding raypaths.

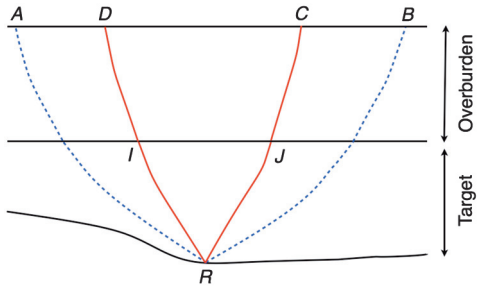

Figure 1. Two-dimensional ray diagram illustrating the PP + PS = SS method for PP and PS reflections from the bottom of the target layer. The wavefield is excited in split-spread geometry by P-wave sources located at points *A* and *B*. Target PP (*ARB*) and PS (*ARC*) events share the downgoing segment *AR*, and therefore, the reflection point *R* at the bottom of the target layer. Another pair of PP (*BRA*) and PS (*BRD*) target events share the downgoing segment *BR*. The constructed SS target event corresponds to *DRC*. P-wave ray segments are marked by dashed blue lines, and S-wave ray segments by solid red lines.

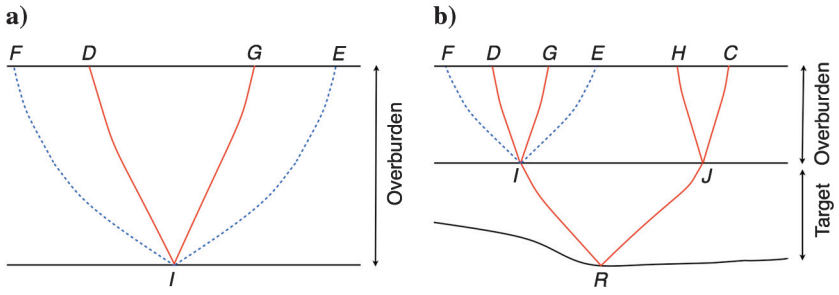

Figure 2. Layer stripping of the constructed SS events. (a) The PP + PS = SS method is applied to kinematically construct pure SS-waves in the overburden. PP (*EIF*) and PS (*EID*) events share the downgoing segment *EI* and the reflection point *I* at the bottom of the overburden. Another pair of PP (*FIE*) and PS (*FIG*) overburden events share the downgoing segment *FI*. The overburden events that share the reflection point *I* are labeled O_1. (b) The constructed overburden SS event *DIG* shares the segment *DI* with the target SS reflection. The overburden events that share the reflection point *J* are labeled O_2.

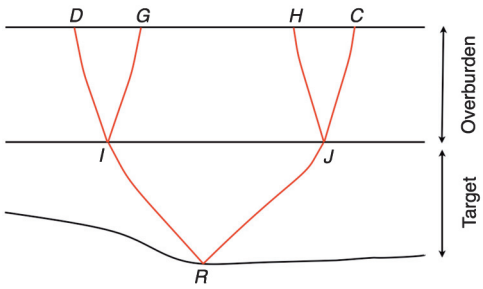

Figure 3. Raypaths of the constructed SS events. The target SS event *DRC* shares the segments *ID* and *JC* with the overburden events *DIG* and *HJC*, respectively. The method produces the interval traveltime along the raypath *IRJ*.

Equations 10 and 11 can be combined to find the attenuation of the constructed shear-wave SS_{01} in the overburden:

$$|U_{SS_{O1}}| = \frac{|U_{PS_{O1}}|^2}{|U_{PP_{O1}}|} = \mathcal{G}_{O1}\, S(\omega)\, e^{-2k^I_{S,O1}\, l_{ID}}, \qquad (12)$$

where $\mathcal{G}_{O1} = \mathcal{G}^2_{PS_{O1}}/\mathcal{G}_{PP_{O1}}$. Likewise, the attenuation coefficient for the overburden event SS_{O2} can be found from

$$|U_{SS_{O2}}| = \frac{|U_{PS_{O2}}|^2}{|U_{PP_{O2}}|} = \mathcal{G}_{O2}\, S(\omega)\, e^{-2k^I_{S,O2}\, l_{JC}}. \qquad (13)$$

The problem of estimating the interval shear-wave attenuation in the target layer (see Figure 3) is now reduced to the attenuation analysis of pure modes considered by Behura and Tsvankin (2009a). Equations 9, 12, and 13 can be combined as follows:

$$|U_{SS_T}| = \frac{|U_{SS_E}|^2}{|U_{SS_{O1}}||U_{SS_{O2}}|} = \mathcal{G}_T\, e^{-2(k^I_{S,DR}\, l_{DR} + k^I_{S,RC} l_{RC}) + 2(k^I_{S,O1} l_{ID} + k^I_{S,O2}\, l_{JC})}, \qquad (14)$$

where $\mathcal{G}_T = \mathcal{G}^2_E/(\mathcal{G}_{O1}\,\mathcal{G}_{O2})$. Because $k^I_{S,DR}\, l_{DR} = k^I_{S,IR}\, l_{IR} + k^I_{S,O1}\, l_{ID}$ and $k^I_{S,RC}\, l_{RC} = k^I_{S,RJ}\, l_{RJ} + k^I_{S,O2}\, l_{JC}$, equation 14 reduces to

$$|U_{SS_T}| = \mathcal{G}_T\, e^{-2k^I_{S,IR}\, l_{IR} - 2k^I_{S,RJ}\, l_{RJ}}. \qquad (15)$$

Taking the logarithm of equation 15 yields:

$$\ln|U_{SS_T}| = \ln \mathcal{G}_T - 2\, k^I_{S,IR}\, l_{IR} - 2\, k^I_{S,RJ}\, l_{RJ} = \ln \mathcal{G}_T - 2\, k^I_{S,T}(l_{IR} + l_{RJ}), \qquad (16)$$

where the coefficient $k^I_{S,T}$ represents the average group attenuation coefficient along the SS-wave raypath in the target layer.

Interval attenuation for a homogeneous target layer

If the target layer is heterogeneous, equation 16 can yield only the offset-dependent average interval S-wave attenuation coefficient, provided the length of the shear-wave raypath ($l_{IR} + l_{RJ}$) is known. Interpretation of attenuation measurements, however, can be significantly simplified for horizontal, homogeneous layers with a horizontal symmetry plane. Then $l_{IR} + l_{RJ} = V_g\, t_{SS_T}$, where V_g is the shear-wave group velocity along the rays *IR* and *RJ* (Figure 3), and t_{SS_T} is the SS-wave interval traveltime in the target layer. As a result, equation 16 reduces to

$$\ln|U_{SS_T}| = \ln \mathcal{G}_T - 2\, k^I_{S,T} V_g\, t_{SS_T}. \qquad (17)$$

Behura and Tsvankin (2009b) show that equation 17 can be used to obtain the phase attenuation coefficient. According to their results,

$$\ln|U_{SS_T}| = \ln \mathcal{G}_T - 2\,\omega\, \mathcal{A}_S\, t_{SS_T}, \qquad (18)$$

where ω is the angular frequency and $\mathcal{A}_S = k^{I,Ph}/k^{R,Ph}$ is the S-wave phase attenuation coefficient (Zhu, 2006); $k^{R,Ph}$ and $k^{I,Ph}$ are the magnitudes of the real and imaginary parts of the wave vector **k**. The angle-dependent quality factor Q_S in anisotropic media is usually defined as $Q_S = 1/(2\,\mathcal{A}_S)$. As proved by Behura and Tsvankin (2009b), the coefficient $\mathcal{A}_S$ in equation 18 has to be evaluated for a zero inhomogeneity angle ξ (the angle between the real and imaginary parts of **k**), irrespective of the actual value of ξ for the ray direction *IR*. In other words, $\mathcal{A}_S$ is found for the imaginary part of **k** aligned with the phase (slowness) direction. This result does not only hold for uncommonly large values of the angle ξ.

The shear-wave interval traveltime in the target layer (t_{SS_T}) is computed from equation 5 using the kinematic layer stripping. Hence, the slope of the logarithmic spectral ratio in equation 18 yields the phase attenuation coefficient $\mathcal{A}_S$ for the phase angle corresponding to the group direction *IR* in Figure 3. If the slope is constant, the coefficient $\mathcal{A}_S$ and the quality factor $Q_S \approx 1/(2\,\mathcal{A}_S)$ are independent of frequency. If the slope varies with frequency, $\mathcal{A}_S$ has to be computed from the instantaneous slope, which yields a frequency-dependent quality factor.

Below we apply our method to estimation of shear-wave interval attenuation coefficients in VTI media and symmetry planes of orthorhombic media. For vertical transverse isotropy, the coefficient $\mathcal{A}_S$ can be inverted for the attenuation anisotropy parameters introduced by Zhu and Tsvankin (2006, 2007). Under the assumptions of weak attenuation and weak velocity and attenuation anisotropy, the SV-wave phase attenuation coefficient is given by (Zhu and Tsvankin, 2006)

$$\mathcal{A}_{SV}(\theta) = \mathcal{A}_{S0}(1 + \sigma_Q \sin^2\theta \cos^2\theta), \qquad (19)$$

$$\sigma_Q = \frac{1}{g_Q}\left[2(1 - g_Q)\sigma + \frac{\epsilon_Q - \delta_Q}{g}\right], \qquad (20)$$

where $\mathcal{A}_{S0} \approx 1/(2\,Q_{S0})$ is the shear-wave symmetry-direction attenuation coefficient (it is the same for SV- and SH-waves), $g_Q = Q_{P0}/Q_{S0}$, Q_{P0} and Q_{S0} are the vertical quality factors for P- and S-waves, respectively, ϵ_Q and δ_Q are the attenuation-anisotropy parameters, $g = V^2_{S0}/V^2_{P0}$, where V_{P0} and V_{S0} are the vertical velocities of P- and S-waves, respectively, $\sigma = (\epsilon - \delta)/g$, and ϵ and δ are the velocity-anisotropy parameters. The parameter σ_Q determines the variation of $\mathcal{A}_{SV}$ away from the symmetry direction.

If the model is orthorhombic and the symmetry of the real and imaginary parts of the stiffness matrix is the same, the VTI equations for the attenuation coefficients can be adapted for the mutually orthogonal symmetry planes (Zhu and Tsvankin, 2007). Here, the symmetry planes of orthorhombic media are taken to coincide with the Cartesian coordinate planes. It should be noted that in-plane polarized SV-waves in the vertical symmetry planes represent two different shear modes, fast S_1 and slow S_2 (Tsvankin, 1997, 2005). Suppose the fast wave S_1 at vertical incidence is polarized in the x_1-direction (i.e., it represents an SV mode in the $[x_1, x_3]$-plane), and the slow wave S_2 in the x_2-direction. Then P-waves are coupled to S_1-waves in the $[x_1, x_3]$-plane and to S_2-waves in the $[x_2, x_3]$-plane.

The linearized SV-wave phase attenuation coefficient in the $[x_1, x_3]$-plane, adapted from equations 19–20, has the form

$$\mathcal{A}^{(2)}_S = \mathcal{A}_{S0}(1 + \sigma^{(2)}_Q \sin^2\theta \cos^2\theta), \qquad (21)$$

where θ is the phase angle with the vertical, $\mathcal{A}_{S0}$ is the vertical attenuation coefficient of the S_1-wave, and $\sigma^{(2)}_Q$ is the SV-wave attenuation-anisotropy parameter in the $[x_1, x_3]$-plane defined by

Zhu and Tsvankin (2007). (The superscript (2) denotes the x_2-axis orthogonal to the $[x_1, x_3]$-plane.) Similarly, the SV-wave attenuation coefficient in the $[x_2, x_3]$ symmetry plane is given by

$$\mathcal{A}_S^{(1)} = \overline{\mathcal{A}}_{S0}(1 + \sigma_Q^{(1)} \sin^2\theta \cos^2\theta), \tag{22}$$

where $\overline{\mathcal{A}}_{S0}$ is the vertical attenuation coefficient of the S_2-wave and $\sigma_Q^{(1)}$ is the corresponding attenuation-anisotropy parameter.

Zhu and Tsvankin (2007) define the *attenuation splitting parameter* $\gamma_Q^{(S)}$ by analogy with the S-wave velocity splitting parameter $\gamma^{(S)}$ as the fractional difference between the attenuation coefficients of the vertically traveling split shear waves:

$$\gamma_Q^{(S)} \equiv \left| \frac{\overline{\mathcal{A}}_{S0} - \mathcal{A}_{S0}}{\mathcal{A}_{S0}} \right|. \tag{23}$$

The coefficient $\gamma_Q^{(S)}$ is expected to play an important role in characterization of fractured reservoirs using shear-wave attenuation measurements.

Inversion of equations 19, 21, and 22 requires knowledge of the phase angle θ corresponding to each source-receiver offset (e.g., to IJ in Figure 3) at the top of the target layer. However, because equations 19, 21, and 22 were derived in the linearized weak-anisotropy approximation, the phase and group angles in the anisotropic terms are interchangeable. Therefore, the angle θ can be replaced with the corresponding group angle computed from the known offset using an approximate thickness of the target layer.

SYNTHETIC EXAMPLES

Layered VTI media

The method was first tested on synthetic multicomponent data from a horizontally layered VTI model (Figure 4). The source was placed at the top of the model, and the receivers were at the water bottom. Our method is applicable to this source-receiver geometry because it utilizes events with shared ray segments in the overburden.

Synthetic reflection data were generated by using an anisotropic reflectivity code (Schmidt and Tango, 1986). The interval parameters for the model (Table 1) were chosen so as to simulate significant P- and S-wave attenuation and attenuation anisotropy. A broadband (0.1 – 150 Hz) source wavelet employed in the reflectivity method ensured that the spectral-ratio method could operate with a sufficient number of frequencies. The PP and PS events from the top and bottom of the third (target) layer were identified on the vertical and radial displacement components of the shot gather (Figure 5). Kinematic layer stripping of the shear-wave traveltimes (equation 5) produced the interval moveout in the target layer shown in Figure 6. The layer-stripped interval traveltimes practically coincide with the exact values computed by ray tracing. It should be noted that the maximum offset for the constructed shear-wave in the target layer is limited by the critical angle for SP mode conversions, which is equal to 32°. The critical angle, however, is reached only for infinitely large offsets of the acquired PP- and PS-waves.

The input amplitudes were obtained by computing the vector sum of the radial and vertical displacement components. Frequency-domain amplitudes were found by putting a tapered cosine window (with a length of 128 time samples) around the arrivals and applying the Fourier transform. The target layer is horizontal, homogeneous,

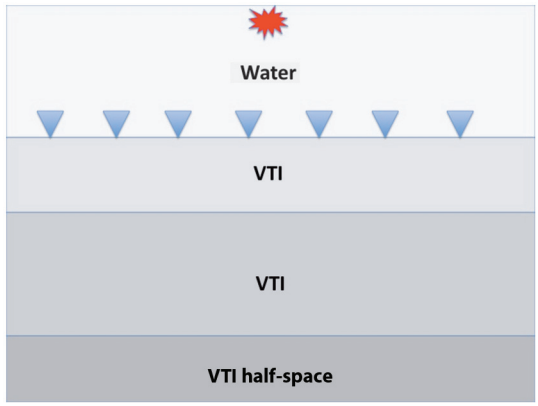

Figure 4. Synthetic model used to test the algorithm. The source is at the surface and the receivers are at the water bottom. The model parameters are listed in Table 1.

Table 1. Synthetic model used to estimate SV-wave interval attenuation in VTI media.

	Layer 1	Layer 2	Layer 3	Halfspace
Symmetry	Isotropic	VTI	VTI	VTI
d (km)	2.00	0.60	1.00	—
V_{P0} (km/s)	1.50	1.60	1.70	2.00
V_{S0} (km/s)	—	0.80	0.90	1.20
ϵ	—	0.30	0.25	0.40
δ	—	0.10	0.10	0.20
σ	—	0.80	0.54	0.56
Q_{P0}	—	50	100	60
Q_{S0}	—	50	20	70
ϵ_Q	—	0.30	0.20	0.40
δ_Q	—	0.20	0.10	0.30
σ_Q	—	0.40	−0.78	0.08

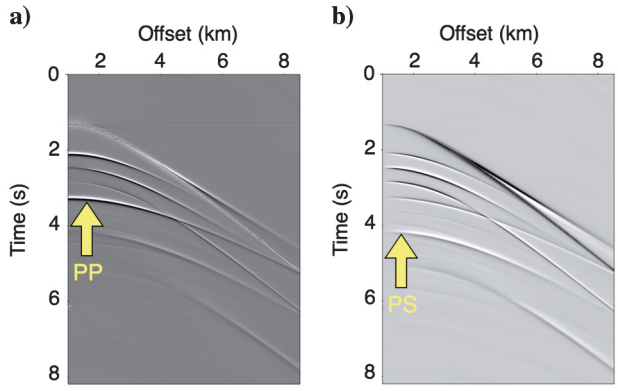

Figure 5. (a) Vertical and (b) horizontal displacement components of a shot gather for the model from Figure 4. The PP (a) and PS (b) reflections from the bottom of the target (third) layer are marked by arrows.

and (as any VTI medium) has a horizontal plane of symmetry. Therefore, the interval shear-wave phase attenuation coefficient in the target was computed from equation 18 by using the algorithm discussed above. Attenuation coefficients for offsets corresponding to spectral contamination by multiples were removed. The SV-wave phase angles were obtained from the corresponding group angles using the known velocity function in the target layer. The parameters $\mathcal{A}_{S0} = 0.025 \pm 10^{-4}$ and $\sigma_Q = -0.72 \pm 0.20$ were found by least-squares fitting of equation 19 to the estimated shear-wave phase attenuation coefficient $\mathcal{A}_{SV}$ (Figure 7), with the error bars corresponding to the standard deviations from the best-fit function. The inverted parameter $\mathcal{A}_{S0}$ practically coincides with its actual value, but there is a significant uncertainty in the estimate of σ_Q (the actual value is -0.78) due to the limited range of phase angles for the reflected S-leg of the PS-wave and the small PS-wave reflection coefficient at near-vertical incidence. For this model, equation 19 provides a close approximation to the exact attenuation coefficient.

Then, we added Gaussian noise to the radial and vertical displacement components of the PP- and PS-events, which resulted in a signal-to-noise ratio of 2.5. The bandwidth used in the spectral-ratio method has to be chosen in a frequency range where the signal-to-noise ratio is sufficiently high. To obtain a robust estimate of the slope from the logarithmic spectral ratio, we employed the iteratively reweighted least-squares method (Scales and Gersztenkorn, 1988; Aster et al., 2005). The inversion for the attenuation coefficients was performed for 100 realizations of Gaussian noise. The obtained mean values and pooled standard deviations of the coefficients are $\mathcal{A}_{S0} = 0.0246 \pm 2 \times 10^{-4}$ and $\sigma_Q = -0.60 \pm 0.30$. Therefore, the estimate of $\mathcal{A}_{SO}$ is accurate, whereas the coefficient σ_Q is somewhat biased.

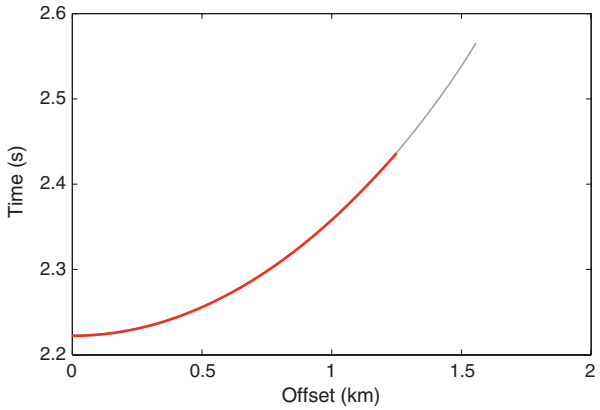

Figure 6. Shear-wave interval traveltime (red dots) in the target layer computed using the PP + PS = SS method and velocity-independent layer stripping. The gray curve marks the exact traveltime.

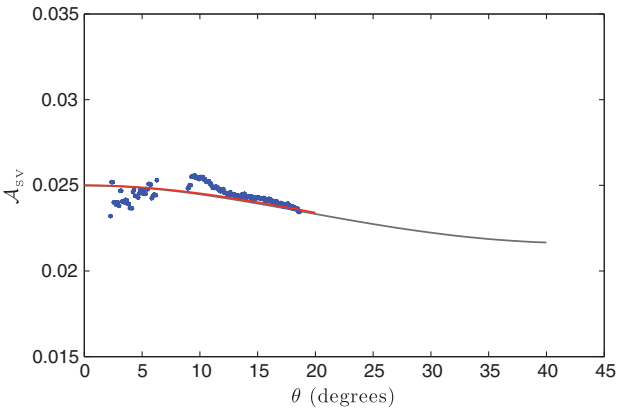

Figure 7. Estimated SV-wave interval phase attenuation coefficient $\mathcal{A}_{SV}$ in the target layer (blue dots) as a function of the phase angle θ. Attenuation coefficients corresponding to spectral contamination by multiples have been removed. The red and gray lines are the best-fit and exact coefficients $\mathcal{A}_{SV}$, respectively.

Symmetry planes of layered orthorhombic media

Next, we consider a model that includes two horizontal orthorhombic layers with aligned vertical symmetry planes (Table 2). The acquisition geometry shown in Figure 4 was used to generate synthetic data in the vertical symmetry planes $[x_1, x_3]$ and $[x_2, x_3]$ with the same anisotropic reflectivity code. The 2D version of our method for estimating interval attenuation is entirely valid in both vertical symmetry planes, if the symmetry-plane azimuths do not vary with depth. In contrast to VTI media, geometric spreading in orthorhombic media is influenced by azimuthal velocity variations even within the symmetry planes (Tsvankin, 2005, Chapter 2).

Table 2. Synthetic model used to estimate shear-wave interval attenuation in symmetry planes of orthorhombic media. The vertical symmetry planes in layers 2–4 are aligned.

	Layer 1	Layer 2	Layer 3	Halfspace
Symmetry	Isotropic	Orthorhombic	Orthorhombic	Orthorhombic
d (km)	2.00	0.60	1.00	—
V_{P0} (km/s)	1.50	1.60	1.70	2.50
V_{S0} (km/s)	—	0.80	1.00	1.40
$\epsilon^{(2)}$	—	0.25	0.40	0.30
$\delta^{(2)}$	—	0.10	0.30	0.10
$\sigma^{(2)}$	—	0.60	0.29	0.64
$\epsilon^{(1)}$	—	0.30	0.20	0.40
$\delta^{(1)}$	—	0.15	0.10	0.30
$\sigma^{(1)}$	—	0.65	0.43	0.38
$\gamma^{(S)}$	—	0.04	0.25	0.10
Q_{P0}	—	40	50	60
Q_{S0}	—	40	30	50
$\epsilon_Q^{(2)}$	—	−0.20	0.30	0.40
$\delta_Q^{(2)}$	—	−0.10	−0.20	0.30
$\sigma_Q^{(2)}$	—	−0.32	0.64	0.05
$\epsilon_Q^{(1)}$		−0.30	0.25	0.40
$\delta_Q^{(1)}$	—	−0.20	−0.15	0.30
$\sigma_Q^{(1)}$	—	−0.58	1.22	0.38
$\gamma_Q^{(S)}$	—	0.12	0.34	0.17

The geometric-spreading factor, however, is treated as part of the frequency-independent term of the amplitude function and does not influence inverted attenuation coefficients.

The synthetic data in the planes $[x_1, x_3]$ and $[x_2, x_3]$ (Figures 8 and 9) were processed separately. As discussed above, for symmetry-plane propagation the P-wave is coupled only to the in-plane polarized SV-wave (either S_1 or S_2). Therefore, only one mode conversion (PS_1 or PS_2) is recorded in each vertical symmetry plane. Due to shear-wave splitting at vertical incidence, the near-offset PS_1 and PS_2 reflections are shifted with respect to each other in time. The interval SS-wave moveout functions in the symmetry planes computed for the third (target) layer by kinematic layer stripping are close to the exact traveltimes (Figure 10). The critical angle for SP mode conversions, which restricts the offset range of the constructed SS-waves, is equal to 26° in the $[x_1, x_3]$-plane and 24° in the $[x_2, x_3]$-plane.

To estimate the attenuation parameters, we performed least-squares fitting of equations 21 and 22 to the computed symmetry-plane shear-wave interval attenuation coefficients (Figure 11). The obtained vertical attenuation coefficients $\mathcal{A}_{S0} = 0.0165 \pm 10^{-4}$ and $\overline{\mathcal{A}}_{S0} = 0.0124 \pm 3 \times 10^{-4}$ barely deviate from the actual parameters ($\mathcal{A}_{S0} = 0.0167$, $\overline{\mathcal{A}}_{S0} = 0.0125$). Consequently, the method yields a highly accurate attenuation splitting parameter ($\gamma_Q^{(S)} = -0.33$). As is the case for the VTI model, the attenuation-anisotropy parameters $\sigma_Q^{(2)}$ and $\sigma_Q^{(1)}$ are more distorted and have larger standard deviations.

DISCUSSION

Despite the generally successful test results, the proposed method has several limitations. First, the range of phase angles for the constructed SS-wave is restricted due to two factors: the small amplitudes of PS-waves at near offsets and the critical angle for converted waves. The critical angle seldom exceeds 30°–35°, which may cause instability in the inversion for the attenuation-anisotropy parameter σ_Q in VTI media and parameters $\sigma_Q^{(1,2)}$ in orthorhombic media. Estimation of σ_Q should be more accurate for hard rocks with high V_S/V_P ratios, for which the critical angle for SP mode conversions is larger. However, the algorithm should provide tight constraints on the vertical attenuation coefficients and, therefore, on the attenuation splitting parameter for orthorhombic media. Second, because the data are generated by a P-wave source, it is necessary to repeatedly apply the PP + PS = SS method to construct SS events, which could lead to error accumulation in the attenuation analysis. Third, the algorithm assumes that the source radiation pattern and the receiver directivity function are frequency independent (equation 9). This assumption is valid for point sources in weakly heterogeneous anisotropic media, if attenuation-related velocity dispersion in the seismic frequency band can be ignored. However, source and receiver arrays in particular acquisition geometries can produce a frequency-dependent directivity function, which may distort attenuation coefficients measured by the spectral-ratio method (Hustedt and Clark, 1999) or produce "artificial" attenuation-anisotropy signatures (Vasconcelos and Jenner, 2005).

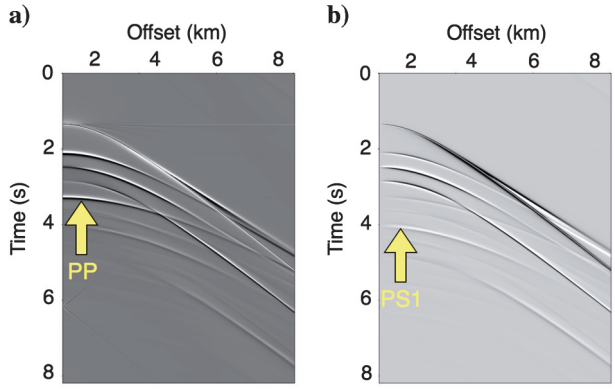

Figure 8. (a) Vertical and (b) horizontal displacement components of a shot gather in the $[x_1, x_3]$-plane of the model from Table 2. The PP and PS reflections from the bottom of the target (third) layer are marked by arrows.

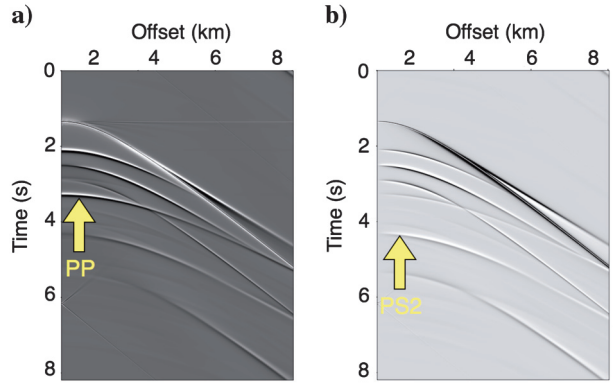

Figure 9. (a) Vertical and (b) horizontal displacement components of a shot gather in the $[x_2, x_3]$-plane of the model from Table 2. The PP and PS reflections from the bottom of the target layer are marked by arrows.

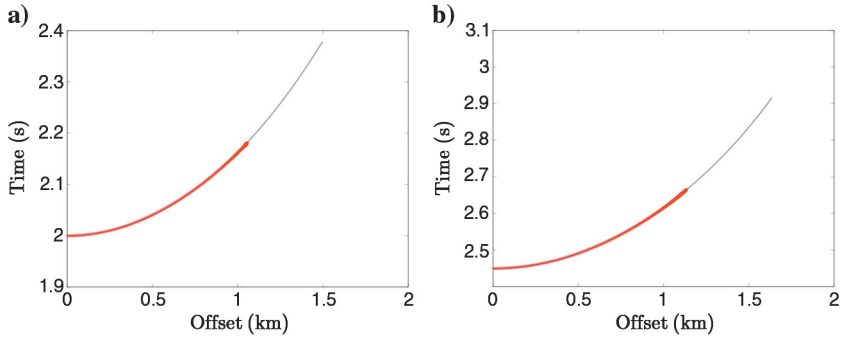

Figure 10. Interval traveltimes (red dots) of the in-plane polarized S-wave in the target (third) layer computed using the PP + PS = SS method and velocity-independent layer-stripping for (a) $[x_1, x_3]$-plane and (b) $[x_2, x_3]$-plane. The gray curves mark the exact traveltimes.

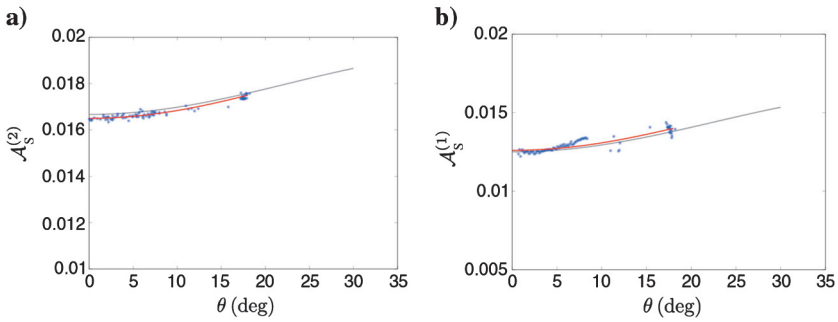

Figure 11. Estimated S-wave interval phase attenuation coefficient $\mathcal{A}_{SV}$ (blue dots) in the third layer as a function of the phase angle θ for (a) $[x_1, x_3]$-plane and (b) $[x_2, x_3]$-plane. Attenuation coefficients corresponding to spectral contamination by multiples have been removed. The red and gray lines are the best-fit and exact attenuation coefficients. The best-fit parameters are $\mathcal{A}_{S0} = 0.0165 \pm 10^{-4}$, $\overline{\mathcal{A}}_{S0} = 0.0124 \pm 3 \times 10^{-4}$, $\sigma_Q^{(2)} = 0.70 \pm 0.25$, and $\sigma_Q^{(1)} = 1.30 \pm 0.40$. The actual values are $\mathcal{A}_{S0} = 0.0167$, $\overline{\mathcal{A}}_{S0} = 0.0125$, $\sigma_Q^{(2)} = 0.64$, and $\sigma_Q^{(1)} = 1.22$.

Application of the algorithm to field data requires registration (correlation) of PP and PS data sets to identify reflections from the same interfaces. Then the traveltimes of the overburden and target PP and PS events can be found by nonhyperbolic semblance analysis (Vasconcelos and Tsvankin, 2006; Xu and Tsvankin, 2008). Kinematic layer stripping for both 2D data and 3D wide-azimuth surveys can be implemented by using the methodology of Wang and Tsvankin (2009).

As in the above synthetic example, the input amplitudes have to be found in a suitable time window around reflection arrivals. Because the algorithm is supposed to operate with isolated reflection events, amplitude distortions due to interference (e.g., with multiples) would hinder S-wave attenuation estimates. The impact of such interference may be mitigated by employing variable-window time-frequency transforms (Reine et al., 2009b). Appropriate smoothing filters in the frequency domain should help reduce errors in spectral-ratio estimates produced by notches in amplitude spectra. If lateral heterogeneity is relatively weak, the algorithm can benefit from data redundancy because the attenuation coefficients for fixed offset and azimuth can be estimated from multiple traces.

Expressing $\mathcal{A}_{SV}$ as a function of the phase angle (equation 19) requires knowledge of the velocity function. However, as discussed by Behura and Tsvankin (2009a), the difference between the phase and group angles for moderately anisotropic models does not substantially distort attenuation coefficients. It should be mentioned, however, that even the group angle for a given source-receiver pair cannot be computed without depth information, which can be approximately obtained from hyperbolic moveout analysis of the interval shear-wave traveltimes.

CONCLUSIONS

We extended the algorithm of Behura and Tsvankin (2009a), originally introduced for pure modes, to the combination of PP- and PS-waves with the goal of estimating the shear-wave interval attenuation coefficient. Our technique involves repeated application of the PP + PS = SS method followed by velocity-independent layer stripping (VILS), for both traveltime and frequency-domain amplitudes. In the 2D implementation of the method discussed here, the vertical incidence plane has to be a plane of mirror symmetry in all layers including the target horizon. VILS is designed for a laterally homogeneous (although possibly vertically heterogeneous) overburden with a horizontal symmetry plane in each layer. If this assumption is satisfied, our method does not require knowledge of the overburden velocity and attenuation parameters.

For heterogeneous target layers, the algorithm estimates the average S-wave interval group attenuation coefficient for a range of source-receiver offsets. If the target is horizontal, homogeneous, and has a horizontal symmetry plane, it is possible to obtain the offset-dependent interval phase attenuation coefficient for the constructed SS events.

Synthetic modeling for layered VTI and orthorhombic media confirmed the accuracy of the method in estimating the interval SV-wave phase attenuation coefficient $\mathcal{A}_{SV}$. The range of phase angles for the constructed SS reflection is limited by the small amplitudes of PS-waves at near offsets and the critical angle for the reflected S-leg. The coefficient $\mathcal{A}_{SV}$ can be inverted for the symmetry-direction coefficient $\mathcal{A}_{S0}$ for VTI media and the vertical attenuation coefficients of the split S-waves for orthorhombic media. Therefore, application of the method to azimuthally anisotropic media helps evaluate the attenuation splitting parameter $\gamma_Q^{(S)}$, which may carry important information about fracturing. Under favorable circumstances (i.e., for long-offset data and layers with a relatively large V_S/V_P ratio), it may be possible to constrain the anisotropy parameters responsible for the variation of the SS-wave attenuation coefficient away from the vertical.

Joint analysis of the P- and S-wave attenuation coefficients can be used to detect the presence of fluids in a reservoir. In combination with the shear-wave velocity splitting parameter $\gamma^{(S)}$, its attenuation counterpart $\gamma_Q^{(S)}$ could serve as a potentially valuable fracture-detection attribute.

ACKNOWLEDGMENTS

We are grateful to the members of the A(nisotropy)-Team of the Center for Wave Phenomena (CWP), Colorado School of Mines, for fruitful discussions. We would like to thank associate editor Mirko van der Baan and reviewers Carl Reine and Ludmila Adam for their constructive suggestions. Support for this work was provided by the Consortium Project on Seismic Inverse Methods for Complex Structures at CWP and by the Research Partnership to Secure Energy for America (RPSEA).

REFERENCES

Adam, L., M. Batzle, K. Lewallen, and K. V. Wijk, 2009, Seismic wave attenuation in carbonates: Journal of Geophysical Research, **114**, B06208, doi: 10.1029/2008JB005890.

Aster, R. C., B. Borchers, and C. H. Thurber, 2005, Parameter estimation and inverse problems: Elsevier.

Batzle, M., R. Hofmann, and M. Prasad, 2005, Seismic attenuation: Observations and mechanisms: 75th Annual International Meeting, SEG, Expanded Abstracts, 1565–1568.

Behura, J., M. Batzle, R. Hofmann, and J. Dorgan, 2007, Heavy oils: Their shear story: Geophysics, **72**, no. 5, E175–E183, doi: 10.1190/1.2756600.

Behura, J., and I. Tsvankin, 2009a, Estimation of interval anisotropic attenuation from reflection data: Geophysics, **74**, no. 6, A69–A74, doi: 10.1190/1.3191733.

Behura, J., and I. Tsvankin, 2009b, Role of the inhomogeneity angle in anisotropic attenuation analysis: Geophysics, **74**, no. 5, WB177–WB191, doi: 10.1190/1.3148439.

Blanchard, T., M. van der Baan, R. Clark, and B. Kurmashov, 2010, P-wave attenuation as an additional tool for monitoring CO_2 injection sites: 80th Annual International Meeting, SEG, Expanded Abstracts, 4252–4256.

Carcione, J., 1992, Anisotropic *Q* and velocity dispersion of finely layered media: Geophysical Prospecting, **40**, 761–783, doi: 10.1111/gpr.1992.40.issue-7.

Chapman, M., 2003, Frequency-dependent anisotropy due to meso-scale fractures in the presence of equant porosity: Geophysical Prospecting, **51**, 369–379, doi: 10.1046/j.1365-2478.2003.00384.x.

Chichinina, T., I. Obolentseva, L. Gik, B. Bobrov, and G. Ronquillo-Jarillo, 2009, Attenuation anisotropy in the linear-slip model: Interpretation of physical modeling data: Geophysics, **74**, no. 5, WB165–WB176, doi: 10.1190/1.3173806.

De, G. S., D. F. Winterstein, and M. A. Meadows, 1994, Comparision of P- and S-wave velocities and Q's from VSP and sonic log data: Geophysics, **59**, 1512–1529, doi: 10.1190/1.1443541.

Dellinger, J., S. Brandsberg-Dahl, R. Clarke, and L. Thomsen, 2002, Alford rotation after tensor migration: 72nd Annual International Meeting, SEG, Expanded Abstracts, 982–985.

Dewangan, P., and I. Tsvankin, 2006, Velocity-independent layer stripping of PP and PS reflection traveltimes: Geophysics, **71**, no. 4, U59–U65, doi: 10.1190/1.2210975.

Gaiser, J. E., 1997, 3-D converted shear wave rotation with layer stripping: U.S. Patent 5,610,875.

Grechka, V., and P. Dewangan, 2003, Generation and processing of pseudo-shear-wave data: Theory and case study: Geophysics, **68**, 1807–1816, doi: 10.1190/1.1635033.

Grechka, V., and I. Tsvankin, 2002, PP + PS = SS: Geophysics, **67**, 1961–1971, doi: 10.1190/1.1527096.

Hustedt, B., and R. A. Clark, 1999, Source/receiver array directivity effects on marine seismic attenuation measurements: Geophysical Prospecting, **47**, 1105–1119, doi: 10.1046/j.1365-2478.1999.00169.x.

Johnston, D. H., and M. Toksöz, 1981, Seismic wave attenuation: SEG, Geophysics reprint series.

Klimentos, T., 1995, Attenuation of P- and S-waves as a method of distinguishing gas and condensate from oil and water: Geophysics, **60**, 447–458, doi: 10.1190/1.1443782.

Liu, E., M. Chapman, I. Varela, X. Li, J. H. Queen, and H. Lynn, 2007, Velocity and attenuation anisotropy: Implication of seismic fracture charecterizations: The Leading Edge, **26**, 1170–1174, doi: 10.1190/1.2780788.

Prasad, M., and A. Nur, 2003, Velocity and attenuation anisotropy in reservoir rocks: 73rd Annual International Meeting, SEG, Expanded Abstracts, 1652–1655.

Reine, C. A., R. A. Clark, and M. van der Baan, 2009a, Interval-Q measurements from surface seismic data using a robust prestack inversion algorithm: 71st EAGE Annual Conference.

Reine, C. A., M. van der Baan, and R. Clark, 2009b, The robustness of seismic attenuation measurements using fixed- and variable-window time-frequency transforms: Geophysics, **74**, no. 2, WA123–WA135, doi: 10.1190/1.3043726.

Scales, J. A., and A. Gersztenkorn, 1988, Robust methods in inverse theory: Inverse Problems, **4**, 1071–1091, doi: 10.1088/0266-5611/4/4/010.

Schmidt, H., and G. Tango, 1986, Efficient global matrix approach to the computation of synthetic seismograms: Geophysical Journal of the Royal Astronomical Society, **84**, 331–359.

Simmons, J. L., 2009, Converted-wave splitting estimation and compensation: Geophysics, **74**, no. 1, D37–D48, doi: 10.1190/1.3036009.

Tsvankin, I., 1997, Anisotropic parameters and P-wave velocity for orthorhombic media: Geophysics, **62**, 1292–1309, doi: 10.1190/1.1444231.

Tsvankin, I., 2005, Seismic signatures and analysis of reflection data in anisotropic media, 2nd ed.: Elsevier.

Vasconcelos, I., and E. Jenner, 2005, Estimation of azimuthally varying attenuation from wide-azimuth P-wave data: 75th Annual International Meeting, SEG, Expanded Abstracts, 123–126.

Vasconcelos, I., and I. Tsvankin, 2006, Nonhyperbolic moveout inversion of wide-azimuth P-wave data for orthorhombic media: Geophysical Prospecting, **54**, 535–552, doi: 10.1111/j.1365-2478.2006.00559.x.

Wang, X., and I. Tsvankin, 2009, Estimation of interval anisotropy parameters using velocity-independent layer stripping: Geophysics, **74**, no. 5, WB117–WB127, doi: 10.1190/1.3157462.

Xin, K., B. Hung, S. Birdus, and J. Sun, 2008, 3-D tomographic amplitude inversion for compensating amplitude attenuation in the overburden: 78th Annual International Meeting, SEG, Expanded Abstracts, 3239–3243.

Xu, X., and I. Tsvankin, 2008, Moveout-based geometrical-spreading correction for PS-waves in layered anisotropic media: Journal of Geophysics and Engineering, **5**, 195–202, doi: 10.1088/1742-2132/5/2/006.

Zhu, Y., 2006, Seismic wave propagation in attenuative anisotropic media: Ph.D. thesis, Colorado School of Mines.

Zhu, Y., and I. Tsvankin, 2006, Plane-wave propagation in attenuative transversely isotropic media: Geophysics, **71**, no. 2, T17–T30, doi: 10.1190/1.2187792.

Zhu, Y., and I. Tsvankin, 2007, Plane-wave attenuation anisotropy in orthorhombic media: Geophysics, **72**, no. 1, D9–D19, doi: 10.1190/1.2387137.

Zhu, Y., I. Tsvankin, and I. Vasconcelos, 2007, Effective attenuation anisotropy of thin-layered media: Geophysics, **72**, no. 5, D93–D106, doi: 10.1190/1.2754185.